Physics of Fluids

Optimal chordwise stiffness distribution for self-propelled heaving flexible plates

Cite as: Phys. Fluids **32**, 111905 (2020); https://doi.org/10.1063/5.0029806
Submitted: 16 September 2020 . Accepted: 29 October 2020 . Published Online: 13 November 2020

Wenjiang Wang, Haibo Huang, and Xi-Yun Lu

View Online Export Citation CrossMark

ARTICLES YOU MAY BE INTERESTED IN

Pulsed-jet propulsion of a squid-inspired swimmer at high Reynolds number
Physics of Fluids **32**, 111901 (2020); https://doi.org/10.1063/5.0027992

Specialization of tuna: A numerical study on the function of caudal keels
Physics of Fluids **32**, 111902 (2020); https://doi.org/10.1063/5.0029340

On the near-wall structures and statistics of fluctuating pressure in compressible turbulent channel flows
Physics of Fluids **32**, 115121 (2020); https://doi.org/10.1063/5.0024639

AIP Advances
Fluids and Plasmas Collection
READ NOW

© 2020 Author(s).

Physics of Fluids ARTICLE scitation.org/journal/phf

Optimal chordwise stiffness distribution for self-propelled heaving flexible plates

Cite as: Phys. Fluids 32, 111905 (2020); doi: 10.1063/5.0029806
Submitted: 16 September 2020 • Accepted: 29 October 2020 •
Published Online: 13 November 2020

View Online Export Citation CrossMark

Wenjiang Wang, Haibo Huang,[a] and Xi-Yun Lu

AFFILIATIONS

Department of Modern Mechanics, University of Science and Technology of China, Hefei, Anhui 230026, China

[a]Author to whom correspondence should be addressed: huanghb@ustc.edu.cn

ABSTRACT

The effect of non-uniform chordwise stiffness distribution on the self-propulsive performance of three-dimensional flexible plates is studied numerically. Some typical stiffness distributions, including uniform, declining, and growing distribution, are considered. First, the normalized bending stiffness $\widetilde{K}$ is derived, which can well represent the overall bending stiffness of the non-uniform plates. For different non-uniformly distributed plates with the same $\widetilde{K}$, the maximum displacement difference between the trailing and leading edges of the plate during the flapping is almost identical. There exists a common optimal $\widetilde{K}$ at which all the plates achieve their optimal performance, i.e., the highest cruising speed and efficiency. Second, we reveal what kind of non-uniform distribution could be the best at a specific $\widetilde{K}$ in terms of the propulsive performance. The force analysis indicates that a larger bending deformation in the anterior part for the growing distribution leads to a larger thrust. Hence, the large local slope along the anterior flexible plate is preferred to enhance the propulsive performance. The results obtained in this study may shed some light on a better understanding of the hydrodynamic effect on the self-propulsion of the non-uniform stiffness wings or fins of animals.

Published under license by AIP Publishing. https://doi.org/10.1063/5.0029806

I. INTRODUCTION

Flapping is one of the most prevalent modes of biological propulsion, for example, fish flap their tail fins and birds flap their wings to obtain thrust in cruise. In the flapping procedure, they drive the surrounding viscous fluid flow backwards to push themselves forward. In this procedure, the flexibility of the propulsors (tail fins and wings) may significantly improve the thrust of swimming and flying.[1,2] Self-propulsion of the flexible propulsor is more complex than that of a rigid one because the fluid force, structural force, inertial force, and other factors are coupled.[3–8]

To explore the effect of fin or wing flexibility on the propulsive and maneuvering performance of fishes or birds, a variety of studies have been carried out. Among them, theoretical works[9–11] have investigated the effect of flexibility on the propulsion performance of plates. Through experiments and theoretical analysis of a self-propelled flexible foil in an inviscid fluid, Alben *et al.*[10] found that the cruising speed of the foil is a function of foil length and rigidity. Moore[11] proposed a small-amplitude theory to model a flapping wing with passive pitching due to the combination of wing compliance, inertia, and fluid. They found dramatic performance improvements when the wing is driven near resonance forces. Furthermore, the experimental investigations[12–14] and numerical simulations[9,15–19] indicate that the flexible flapping plate can achieve better performances than the rigid one in terms of propulsive speed and efficiency. Michelin and Llewellyn Smith[20] and Dewey *et al.*[21] have revealed that the peaks of these propulsion characteristics generally appear near the first natural frequency of the propulsor. Hua *et al.*[22] numerically studied the propulsion of a two-dimensional flexible plate heaving in a still fluid. They found that an appropriate rigidity can improve the propulsive performance. In addition, the effect of the trailing-edge shape on the propulsive performance of pitching foils or heaving flexible plates was investigated experimentally[23–25] and numerically.[26,27]

In the studies mentioned above, the models were usually employed by the plates with uniformly distributed rigidity. In reality, however, the wings of birds or the fins of fish are usually non-uniform. For example, there is a decreasing distribution for the stiffness of the caudal fin of fish. The stiffness decreases from the base to the tail due to factors such as muscle system and skeleton frame.[28–30] Due to the influence of bone, vein, and other factors, the stiffness distribution of the wings of birds and insects is also non-uniform.[31,32]

Published under license by AIP Publishing

By observing the swimming and flying of a large number of animals, Lucas *et al.*[33] found that in the process of steady-state flying, their flapping fins and wings have a similar flapping characteristic, whose flexion ratios (length from the propulsor base to the flexion point of bending relative to the total propulsor length) are all about 0.65.

Numerous experimental studies have been carried out on the hydrodynamic performance of the flexible propulsors with non-uniform chordwise flexibility. McHenry *et al.*[28] measured the bending stiffness of the sunfish along the body axis and found that the tail fin is exponentially decreasing. Riggs *et al.*[34] showed that the fin with a biomimetic stiffness profile offers a significant improvement in static thrust, compared to a fin of similar dimensions with a standard NACA0012 airfoil profile. Lucas *et al.*[35] experimentally revealed that the plate with non-uniform stiffness distribution may achieve faster propulsion with higher efficiency and lower consumption. However, only combinations of two segments with different rigidities were considered. It is also noticed that due to the difficulty of experimental measurement and lack of quantitative comparison, little actual biological evidence of the hydrodynamic advantage in the non-uniform flexibility has been found.

Computational fluid dynamics has been a useful tool to investigate the fluid–structure interaction. The effects of different stiffness distributions on propulsion were studied numerically.[36] It has been found that the linear, cubic, and torsional spring distributions are better than the uniform distribution in propulsion performance, and the torsional spring stiffness distribution (or leading-edge concentrated flexibility) is the optimal distribution. On the other hand, Shoele and Zhu[37,38] studied the tail fin and hovering flapping wing, respectively, and concluded that if the leading edge is strengthened, the propulsors may consume less energy and generate more thrust and lift. The aerodynamic characteristics of three-dimensional flexible wings were studied.[39] The flexible wing with the enhanced leading-edge stiffness has a higher average lift–drag ratio and lift–power ratio when it is compared to the rigid or uniformly flexible wings. Peng *et al.*[40] pointed out that the clamped heaving flexible plate with leading-edge strengthening stiffness increases the thrust significantly in the Stokes flow ($Re \sim 0$). Hence, the opinion on the optimal stiffness distribution is contradictory in the literature.

Besides the chordwise flexibility, the spanwise flexibility is another interesting topic, a series of works have been done.[41–44] However, the chordwise flexibility may be more important than that in the spanwise direction because the flow and self-propulsion are in the chordwise direction, and the relevant propulsive performance is desirable to be studied. Luo *et al*[45] studied the effect of the chordwise and spanwise stiffness distributions on the kinematics and propulsion performance of a tuna-like swimmer. Their result confirmed that the chordwise flexibility is more important.

In summary, there have been some studies on the influence of non-uniform chordwise stiffness distribution on propulsive performance. However, there are three limitations to the previous work. First, only simple cases were considered. For example, in the experimental study of Lucas *et al.*,[35] the rigidity distribution is simple since the plate was only composed of two segments with different rigidities. Second, some studies were based on the assumption of inviscid flow and did not consider the significant influence of viscosity[36] or focused on swimming microorganisms, such as spermatozoa or bacteria in the Stokes flow.[40] Finally and most importantly, there is no proper scheme to evaluate the overall rigidity of a non-uniform flexible plate. Actually, only the overall rigidity is correctively evaluated: Can we exclude the effect of different rigidity and further investigate the effect of rigidity distribution? Our study focuses on this point that has never been done before in the literature.

In the present study, we carry out numerical simulations on the locomotion of self-propelled three-dimensional (3D) flexible plates with varying non-uniformly distributed stiffness of the chordwise direction. First, we propose a scheme to evaluate the overall rigidity of a non-uniform plate. Using the equivalent overall rigidity, the performance of non-uniform flexible plates can be compared well. Second, we try to find an optimal non-uniform distribution for a heaving plate and reveal the fundamental mechanisms about how the different stiffness distributions affect the performance of the plates.

The remainder of this paper is organized as follows: The physical problem and mathematical formulation are presented in Sec. II. The numerical method and validation are described in Sec. III. Results are discussed in Sec. IV and concluding remarks are addressed in Sec. V.

II. PHYSICAL PROBLEM AND MATHEMATICAL FORMULATION

A 3D flexible plate with a chord length of c and a span length of b, which is immersed in a stationary fluid, is shown in Fig. 1(a). The leading edge of the plate is forced to heave sinusoidally with

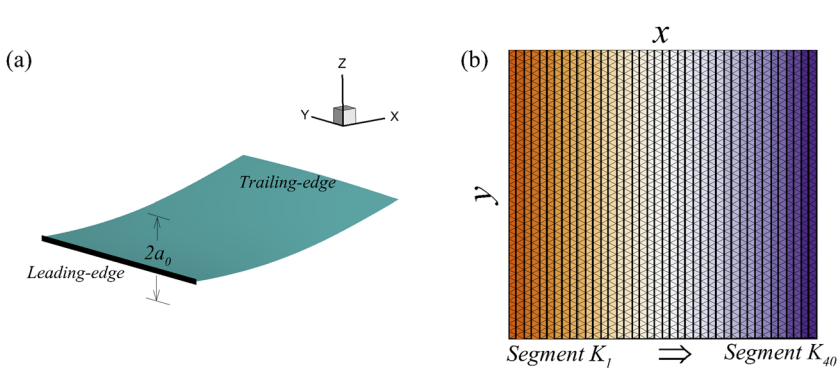

FIG. 1. (a) Schematic diagram of a 3D flexible plate. The leading edge is forced to heave vertically and sinusoidally. The plate deforms passively and moves forward freely. (b) The generated meshes for the plate with 40 segments in different colors.

Published under license by AIP Publishing

oscillating amplitude a_0 and frequency f in the vertical direction. The actuation of the leading edge is described as[20,46,47]

$$h(t) = a_0 \cos(2\pi f t). \tag{1}$$

As a result of the interplay of the plate elasticity, the leading-edge forcing, and the forces exerted by the surrounding fluid, the plate can move forward freely and passively in the stationary fluid (the degree of freedom in the x direction). Meanwhile, only the leading edge of the plate is restricted with a prescribed vertical motion, and the remainder of the plate can deform freely in the entire fluid domain. Here, a Lagrangian coordinate system (s_1, s_2) along the plate surface is defined to describe the configuration and motion of the plate. The fluid flow is governed by the incompressible Navier–Stokes equations,

$$\frac{\partial \boldsymbol{v}}{\partial t} + \boldsymbol{v} \cdot \nabla \boldsymbol{v} = -\frac{1}{\rho}\nabla p + \frac{\mu}{\rho}\nabla^2 \boldsymbol{v} + \boldsymbol{f}, \tag{2}$$

$$\nabla \cdot \boldsymbol{v} = 0, \tag{3}$$

where $\boldsymbol{v}$ is the velocity, p is the pressure, ρ is the density of the fluid, μ is the dynamic viscosity, and $\boldsymbol{f}$ is the Eulerian force acting on the surrounding fluid due to the immersed boundary (IB), as constrained by the no-slip boundary condition. The structural equation is employed to describe the deformation and motion of the plate,[22,48]

$$\rho_s h \frac{\partial^2 \boldsymbol{X}}{\partial t^2} = \sum_{i,j=1}^{2}\left[\frac{\partial}{\partial s_i}\left(Eh\varphi_{ij}\left(\delta_{ij} - \left(\frac{\partial \boldsymbol{X}}{\partial s_i}\cdot\frac{\partial \boldsymbol{X}}{\partial s_j}\right)^{-1/2}\right)\frac{\partial \boldsymbol{X}}{\partial s_j} - \frac{\partial}{\partial s_j}\left(EI\gamma_{ij}\frac{\partial^2 \boldsymbol{X}}{\partial s_i \partial s_j}\right)\right)\right] + \boldsymbol{F}, \tag{4}$$

where $\boldsymbol{X} = (X, Y, Z)$ is the position vector of the plate, $\boldsymbol{F}_s$ is the Lagrangian force exerted on the plate by the fluid, ρ_s is the structural linear mass density of the plate, and h is the thickness of the plate. φ_{ij} is the in-plane effect matrix, where $\varphi_{11} = \varphi_{22} = Eh$ is the stretching stiffness and $\varphi_{12} = Gh$ is the shearing stiffness of the plate. γ_{ij} is the out-of-plane effect matrix, where $\gamma_{11} = \gamma_{22} = \gamma_{12} = EI$ is the bending stiffness of the plate. Besides, δ_{ij} is the Kronecker delta function.

At the leading edge of the plate, the clamped boundary condition is adopted, i.e.,

$$\varphi_{ij}\left(\delta_{ij} - \left(\frac{\partial \boldsymbol{X}}{\partial s_i}\cdot\frac{\partial \boldsymbol{X}}{\partial s_j}\right)^{-1/2}\right)\frac{\partial \boldsymbol{X}}{\partial s_j} - \frac{\partial}{\partial s_j}\left(\gamma_{ij}\frac{\partial^2 \boldsymbol{X}}{\partial s_i \partial s_j}\right) = 0, \tag{5}$$

$$Y(t) = Y(0),\ Z(t) = h(t),\ \frac{\partial \boldsymbol{X}}{\partial s_1} = (1, 0, 0). \tag{6}$$

For the free end of the plate, the boundary condition is

$$\varphi_{ij}\left(\delta_{ij} - \left(\frac{\partial \boldsymbol{X}}{\partial s_i}\cdot\frac{\partial \boldsymbol{X}}{\partial s_j}\right)^{-1/2}\right)\frac{\partial \boldsymbol{X}}{\partial s_j} - \frac{\partial}{\partial s_j}\left(\gamma_{ij}\frac{\partial^2 \boldsymbol{X}}{\partial s_i \partial s_j}\right) = 0, \tag{7}$$

$$\frac{\partial^2 \boldsymbol{X}}{\partial s_i \partial s_j} = 0. \tag{8}$$

The two other free edges $s_2 = 0$ or b are imposed. Here, the Einstein summation convention is not applied on i and j $(i, j = 1, 2)$.

The chord length of the plate c, the heaving frequency f, and the fluid density ρ are used as characteristic quantities to normalize the above equations. It is noted that the characteristic time is $1/f$, i.e., the heaving period. Based on the non-dimensional analysis, there are several dimensionless parameters in our problem: the Reynolds number $Re = \rho f c^2/\mu$, the stretching stiffness $S = Eh/\rho f^2 c^3$, the bending stiffness $K = EI/\rho f^2 c^5$, the mass ratio of the plate and the fluid $M = \rho_s h/\rho c$, the heaving amplitude $A = a_0/c$, and the aspect ratio of the plate $H = b/c$.

To model the non-uniformly distributed stiffness in the present three-dimensional model, the plate is structurally composed of 40 segments in the chordwise direction. Each segment is assigned a unique K_i, as shown in Fig. 1(b). In our study, the distributions of K are considered as follows:

1. Uniform distribution: $K_i = \overline{K}$.
2. Linear distribution: $K_i = \overline{K}(-1.6R_i + 1.8)$, where $R_i = \frac{i}{N}$ and $\frac{N-i}{N}$ for the declining distribution (DD) and growing distribution (GD) cases, respectively.
3. Exponential distribution: $K_i = \overline{K}R_i/R$, where $R_i = e^{-q\frac{i}{N}}$, $R = \int_0^1 e^{(-qx)}\mathrm{d}x$ and $R_i = e^{-q\frac{N-i}{N}}$, $R = \int_0^1 e^{-q(1-x)}\mathrm{d}x$ for the DD and GD cases, respectively, ($q = 1$ and 3.698).

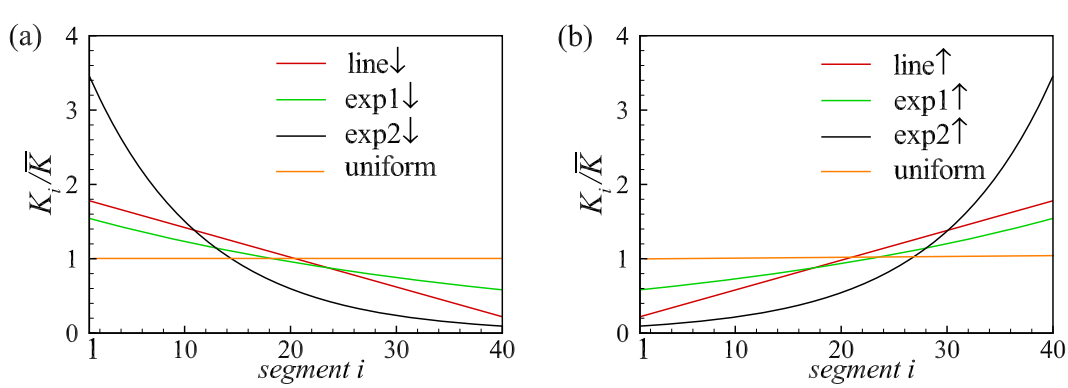

FIG. 2. The distribution patterns of stiffness: (a) declining distribution patterns and (b) growing distribution patterns. The orange line represents the uniform distribution case.

Published under license by AIP Publishing

TABLE I. The nomenclature and standard deviation for typical non-uniformly rigidity distributions (DD—declining distribution and GD—growing distribution).

	$q = 1$	$q = 3.698$	*linear*
DD	exp 1 ↓	exp 2 ↓	*line* ↓
GD	exp 1 ↑	exp 2 ↑	*line* ↑
Standard deviation	$0.286\,26\overline{K}$	$0.937\,97\overline{K}$	$0.467\,62\overline{K}$

Here, DD and GD denote the declining [Fig. 2(a)] and growing distributions [Fig. 2(b)], respectively, from the leading to the trailing edges of the plate. $\overline{K}$ is the arithmetic mean stiffness of all the segments. Especially, the exponential declining distribution $q = 3.698$ is the approximation of the caudal fin of the real sunfish stiffness distribution curve.[34] Ornithopters with a torsional spring[36] is a good example for the GD cases because of the flexibility focusing on the leading part of the wing. To describe the different stiffness distributions more concisely, the nomenclature of the distributions and their standard deviation (SD) are shown in Table I. The symbols ↓ and ↑ denote the DD and GD cases, respectively. The nomenclature exp 1 denotes $q = 1$ and exp 2 denotes $q = 3.698$. At a specific $\overline{K}$, the value of standard deviation exp 2 > *line* > exp 1.

III. NUMERICAL METHOD AND VALIDATION

The governing equations of the fluid–plate problem are solved numerically by an immersed boundary-lattice Boltzmann method for the fluid flow[49] and a finite element method for the motion of the flexible plates.[50] The immersed boundary (IB) method has been extensively applied to problems involving moving boundaries immersed in a viscous fluid flow.[51,52] When the IB method is used to resolve flow–structure interaction, the Lagrangian interaction force $\boldsymbol{F}_s$ in Eq. (4) between the fluid and the immersed boundary can be calculated by the feedback law,[51,52]

$$\boldsymbol{F}_s(s_1, s_2, t) = \alpha \int_0^t [\boldsymbol{V}_f(s_1, s_2, t') - \boldsymbol{V}_s(s_1, s_2, t')]\mathrm{d}t' + \beta[\boldsymbol{V}_f(s_1, s_2, t) - \boldsymbol{V}_s(s_1, s_2, t)], \tag{9}$$

where α and β are free parameters and are selected based on Ref. 22, $\boldsymbol{V}_s = \frac{\partial \boldsymbol{X}}{\partial t}$ is the plate velocity, and the fluid velocity $\boldsymbol{V}_f$ at $\boldsymbol{X}$ is interpolated from the velocities of the surrounding fluid nodes $\boldsymbol{v}$,

$$\boldsymbol{V}_f(s_1, s_2, t) = \int \boldsymbol{v}(x, t)\delta(\boldsymbol{x} - \boldsymbol{X}(s_1, s_2, t)]\mathrm{d}\boldsymbol{x}. \tag{10}$$

In the IB scheme, due to the presence of the plate, the body force $\boldsymbol{f}$ would be exerted on the fluid nodes. In this way, the no-slip boundary condition on the moving plate would be satisfied. The body force $\boldsymbol{f}$ on the Eulerian points (fluid nodes) can be obtained from the Lagrangian force $\boldsymbol{F}_s$ using the Dirac delta function,[51]

$$\boldsymbol{f}(x, t) = -\int \boldsymbol{F}_s(x, t)\delta(\boldsymbol{x} - \boldsymbol{X}(s_1, s_2, t)]\mathrm{d}s_1\mathrm{d}s_2. \tag{11}$$

Furthermore, the lattice Boltzmann equation (LBE) has been widely used to simulate complex flows as an alternative to conventional numerical methods for the Navier–Stokes equations.[22,46,49,53,57] The LBE with the BGK model is

$$f_i(\boldsymbol{x} + \boldsymbol{e}_i\Delta t, t + \Delta t) - f_i(\boldsymbol{x}, t) = -\frac{1}{\tau}[f_i(\boldsymbol{x}, t) - f_i^{eq}(\boldsymbol{x}, t)] + \Delta t F_i \quad (i = 0, 1, \ldots, 18), \tag{12}$$

where τ is the non-dimensional relaxation time related to fluid viscosity, Δt is the time step, and $f_i(\boldsymbol{x}, t)$ is the distribution function associated with discrete particle velocity $\boldsymbol{e}_i$. In our 3D simulations, a D3Q19 velocity model[54] is applied. The equilibrium distribution function f_i^{eq} and the forcing term F_i[55] are defined as

$$f_i^{eq} = \omega_i\rho\left[1 + \frac{\boldsymbol{e}_i \cdot \boldsymbol{v}}{c_s^2} + \frac{\boldsymbol{v}\boldsymbol{v}:(\boldsymbol{e}_i\boldsymbol{e}_i - c_s^2\boldsymbol{I})}{2c_s^4}\right], \tag{13}$$

$$F_i = \left(1 - \frac{1}{2\tau}\right)\omega_i\left[\frac{\boldsymbol{e}_i - \boldsymbol{v}}{c_s^2} + \frac{\boldsymbol{e}_i \cdot \boldsymbol{v}}{c_s^4}\boldsymbol{e}_i\right]\cdot\boldsymbol{f}, \tag{14}$$

where ω_i is the weighting factor and c_s is the speed of sound. The macrovariable velocity $\boldsymbol{v}$ and mass density ρ can be obtained through the distribution functions,

$$\rho = \sum_i f_i, \quad \rho\boldsymbol{v} = \sum_i \boldsymbol{e}_i f_i + \frac{1}{2}\boldsymbol{f}\Delta t. \tag{15}$$

Equation (4) for the deformable plate is discretized by a finite element method and the deformation with large displacement of the plate is handled by the co-rotational scheme.[50] A detailed description of the numerical method can be found in our previous papers.[22,56] A finite moving computational domain is used in the x direction to allow the plate to move for a sufficiently long time. As the plate travels one lattice in the x direction, the computational domain is shifted, i.e., one layer is added at the inlet and another layer is removed at the outlet. Based on our careful validations shown below, the computational domain for the fluid flow is chosen as $[-10, 30] \times [-10, 10] \times [-10, 10]$ in the x, y, and z directions, which is large enough so that the blocking effects of the boundaries are small enough. In the simulations, the Neumann boundary condition $\partial\boldsymbol{v}/\partial x = 0$ is applied at the outlet and the Dirichlet boundary condition $\boldsymbol{v} = 0$ is applied at the inlet and the other four boundaries.

To validate the numerical method used in the present study, a flapping flag in a uniform incoming flow is simulated. The key parameters are $Re = 100$, $M = 1$, $H = 1$, $S = 1000$, and $K = 0.0001$, which are identical to those in the study of Huang and Sung.[58] Figure 3(a) shows the comparison of the present results and the data in the literature. It is seen that both the time-dependent transverse (y direction) displacements at points A (low corner on the trailing edge) and B (midpoint on the trailing edge) in our simulation agree well with those in the study of Huang and Sung.[58]

Grid independence and time step independence studies are also performed. A typical case of a flexible plate with a uniform stiffness was simulated. In the case, the parameters are $A = 0.2$, $M = 0.5$, $K = 2$, $H = 1$, and $Re = 100$. The propulsive velocity of the cases with different mesh sizes and time step size is shown in Fig. 3(b). It is seen that $\Delta x/L = 0.025$ and $\Delta t = 0.000\,25$ are sufficient to achieve accurate results. Here, in all our simulations, $\Delta x/L = 0.025$ and $\Delta t = 0.000\,25$ are adopted.

Published under license by AIP Publishing

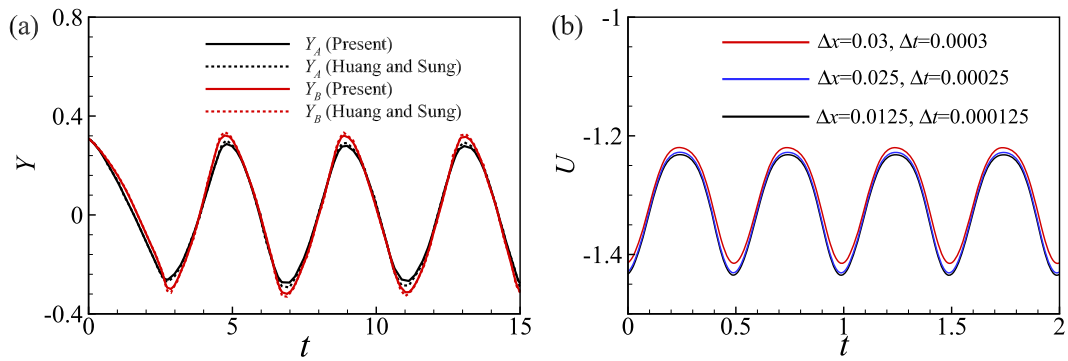

FIG. 3. (a) Time-dependent transverse (y direction) displacements at points A (low corner on the trailing edge) and B (midpoint on the trailing edge). (b) Cruising speed of the flapping flexible plate as a function of time (A = 0.2, M = 0.5, K = 2, H = 1, and Re = 100).

Our numerical strategy has been validated and successfully applied to a wide range of flows, such as the locomotion of a flapping flexible plate,[22] the collective locomotion of two closely spaced self-propelled flapping plates,[46] and the self-propulsion of 3D flexible plates with different trailing-edge shapes.[26]

IV. RESULTS AND DISCUSSION

We present some results on the propulsive behaviors of 3D plates with the non-uniformly distributed stiffness. The parameters are shown in Table II. It is seen that the Reynolds number Re, the stretching stiffness S, the mass ratio M, and the flapping amplitude A are fixed in our simulation. The following two parameters are variables: arithmetic mean bending stiffness $\overline{K}$ and aspect ratio of the plate H. The aspect ratio is fixed to be $H = 1$ if not specified.

A. Propulsive performance

To quantify the propulsive performance of the plates, the mean propulsive velocity, input work, and propulsive efficiency are evaluated. The mean propulsive velocity U is the time-averaged cruising speed at the equilibrium state. The input work W, which is required to actuate the leading edge of the plate, is the time integral of the power P done by the surface of the plate on the surrounding fluid during one flapping period T,

$$W = \int_{t'}^{t'+T} P(t)\mathrm{d}t = \int_{t'}^{t'+T}\left[\int_0^1 \boldsymbol{F}_r(s_1,s_2,t)\frac{\partial \boldsymbol{X}(s_1,s_2,t)}{\partial t}\mathrm{d}s_1\mathrm{d}s_2\right]\mathrm{d}t, \tag{16}$$

TABLE II. The parameters in the simulations.

Reynolds number	Re	100
Mass ratio	M	0.5
Stretching stiffness	S	1000
Arithmetic mean bending stiffness	$\overline{K}$	[0.5, 80]
Flapping amplitude	A	0.25
Aspect ratio	H	1, 4

where $\boldsymbol{F}_r$ is the force on the surrounding fluid by the plate. The propulsive efficiency η is usually defined as the ratio between the kinetic energy of the plate and the input work,

$$\eta = \frac{1}{2}MU^2/W. \tag{17}$$

The normalized time-averaged propulsive velocity U of the plate as a function of $\overline{K}$ is shown in Figs. 4(a) and 4(b). It is seen that all curves increase with $\overline{K}$ first, and after reaching peaks, they decrease with $\overline{K}$. Specifically, for the DD cases [Fig. 4(a)], all curves almost collapse together, and the optimal propulsive performances occur at $\overline{K} \approx 3$. For the GD patterns, the curve of the propulsive velocity U moves right, and the peak increases as the standard deviation (SD) of non-uniformly distributed stiffness increases.

The input work W and the propulsive efficiency η as functions of $\overline{K}$ are shown in Figs. 4(c)–4(f), respectively. Generally speaking, the variation trends of W and η with $\overline{K}$ are consistent with that of U. Two variation modes of U, W, and η as a function of $\overline{K}$ have been identified. At $\overline{K} \approx 3$, the DD plates approximately achieve the best performance. For the GD patterns, the optimal $\overline{K}$ at which the best performance appears increases as the SD of non-uniformly distributed stiffness increases, i.e., the peak moves toward right. Therefore, $\overline{K}$ is not able to reveal the common rules for the performance of the non-uniformly distributed stiffness plates, especially for the GD cases.

B. Normalized bending stiffness $\widetilde{K}$

To better understand the effect of non-uniformly distributed stiffness, here, we derive the normalized bending stiffness to represent the overall bending stiffness of the non-uniform plate. Actually, the flapping plate is similar to a Euler beam with one end fixed and one end free. According to the approximate differential equation of the deflection curve, we have

$$EI(x)\frac{\partial^2 w(x)}{\partial x^2} = -M(x), \qquad x \in [0,1], \tag{18}$$

where $EI(x)$ represents the chordwise bending stiffness distribution with x being the chordwise position, $w(x)$ is the deformed deflection of the plate, and $M(x)$ is the internal moment. The forces experienced by the flapping plates in a viscous incompressible fluid

Published under license by AIP Publishing

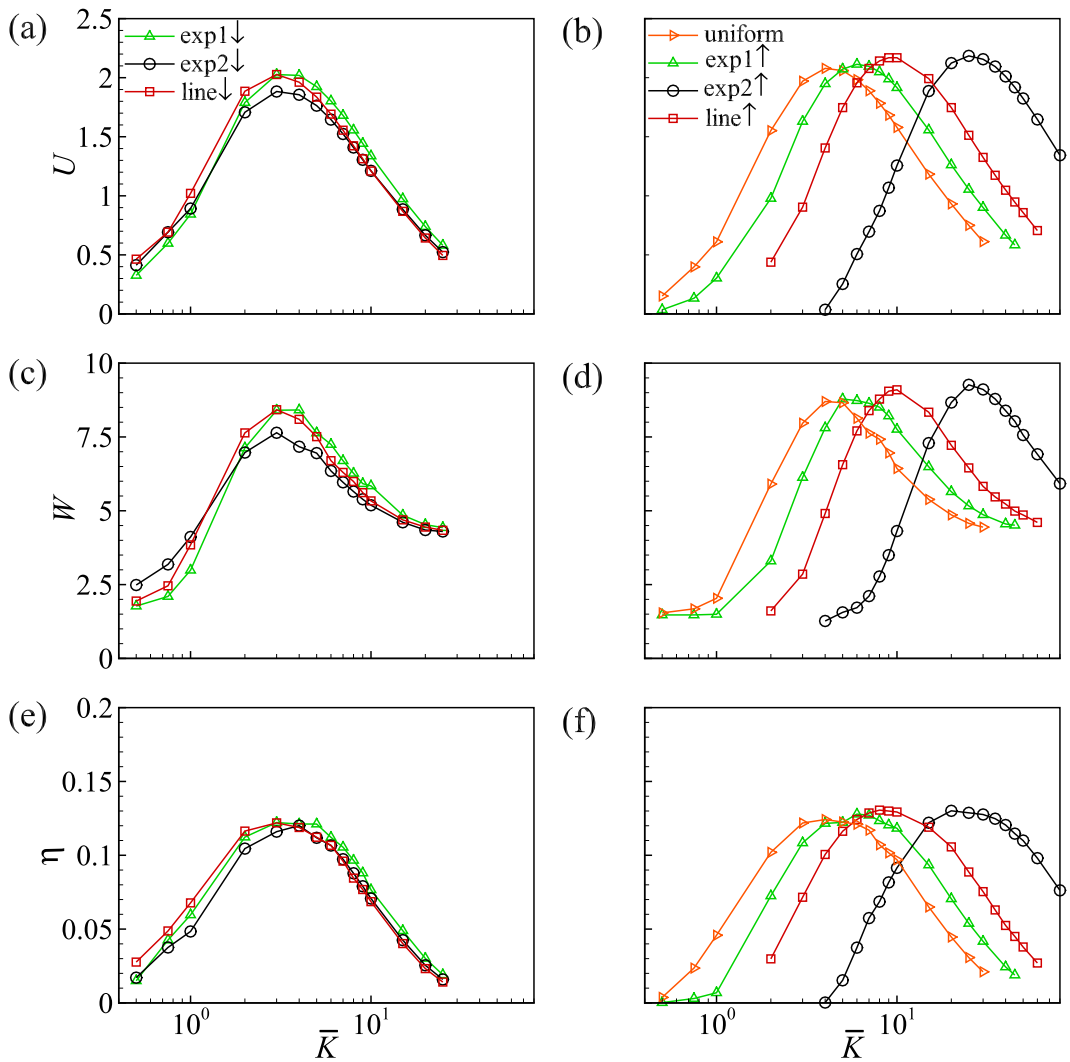

FIG. 4. Propulsive velocity U [(a) and (b)], input work W [(c) and (d)], and propulsive efficiency η [(e) and (f)] as functions of mean bending stiffness $\overline{K}$. (a), (c), and (e) and (b), (d), and (f) are the declining and growing distribution patterns, respectively.

is complex. Previous studies[26,46] have indicated that the bending deformation of a flapping plate is mainly contributed by the normal force. Peng *et al.*[46] have shown that the time-averaged absolute normal force of a heaving flexible plate approximately decreases linearly from the leading to the trailing edges. For simplicity, we suppose that the load distribution along the chordwise direction can be replaced by the normal force distribution. In the normal force model, a unified linear decreasing force distribution is used, where q_0 is the normal force value at the leading edge and zero at the trailing edge. For the beam, the boundary conditions at the leading edge are

$$x = 0, \quad w = 0, \quad \frac{\partial w}{\partial x} = \theta = 0, \tag{19}$$

where θ is the deflection angle.

Integrating Eq. (18), we can get the tail deformed deflection angle,

$$\theta(1) = \frac{\mathrm{d}w}{\mathrm{d}x} = \int_0^1 \frac{-M(x)}{EI(x)}\mathrm{d}x + C. \tag{20}$$

Integrating Eq. (18) twice, we obtain the tail deformed deflection,

$$w(1) = \int_0^1 \int_0^x \left(\frac{-M(x')}{EI(x')}\mathrm{d}x'\right)\mathrm{d}x + Cx + D, \tag{21}$$

where C and D are integral constants.

For the uniformly distributed stiffness, the analytical solution of the tail deformed deflection is

$$w(1) = \frac{q_0}{30\overline{K}}. \tag{22}$$

Published under license by AIP Publishing

TABLE III. $\widetilde{K}$ for typical non-uniformly rigidity distributions.

	exp 1 ↓	exp 2 ↓	*line* ↓	exp 1 ↑	exp 2 ↑	*line* ↑
$\widetilde{K}$	$1.325\,38\overline{K}$	$1.732\,50\overline{K}$	$1.490\,09\overline{K}$	$0.681\,11\overline{K}$	$0.155\,36\overline{K}$	$0.381\,91\overline{K}$

For the typical DD case ($q = 1$),

$$M(x) = -\frac{q_0}{6}(1-x)^3, \quad EI(x) = \overline{K}\frac{e^{-x}}{\int_0^1 e^{-x}\mathrm{d}x}, \quad x \in [0,1]. \tag{23}$$

This yields $w(1) = \frac{q_0}{39.761\,43\overline{K}}$.

Similarly, for the typical GD case ($q = 1$),

$$M(x) = -\frac{q_0}{6}(1-x)^3, \quad EI(x) = \overline{K}\frac{e^{1-x}}{\int_0^1 e^{1-x}\mathrm{d}x}, \quad x \in [0,1]. \tag{24}$$

$w(1)$ can be derived as $\frac{q_0}{20.433\,18\overline{K}}$. It is seen that generally,

$$w(1) = \frac{q_0}{\mu\overline{K}}, \tag{25}$$

where μ is the coefficient for a specific stiffness distribution case. Now, suppose that in all cases, the deformed deflection at the trailing-edge has the same formula as the uniform plate,

$$w(1) = \frac{q_0}{30\widetilde{K}}, \tag{26}$$

where $\widetilde{K}$ is the overall bending stiffness. It is noticed that for the uniform plate, $\widetilde{K} = \overline{K}$. From Eqs. (25) and (26), it yields

$$\widetilde{K} = \frac{\mu\overline{K}}{30}. \tag{27}$$

It is an analogy to converting the form of the deformed deflection expression at all the other cases to the uniformly distributed case. Hence, $\widetilde{K}$ is also a normalized bending stiffness.

Here, $\widetilde{K}$ values for typical rigidity distribution cases are shown in Table III. It is seen that in the DD distribution patterns investigated here, $\widetilde{K}$ is close to each other with a minor difference. However, in the GD patterns, $\widetilde{K}$ decreases as the standard deviation (SD) of the non-uniformly distributed stiffness increases.

We assume that the maximum displacement difference ΔZ between the leading and the trailing edges of the plate during the flapping is proportional to the derived tail deformed deflection of the plate $w(1)$. Through our numerical simulations, we obtain ΔZ as a function of $\overline{K}$ and $\widetilde{K}$ for different distributions [see Figs. 5(a) and 5(b)]. It is seen that at a specific $\overline{K}$, different distribution has different ΔZ. It seems that using $\overline{K}$, the curves are not well normalized. On the other hand, if $\widetilde{K}$ is used, the curves of different distribution patterns almost collapse together [see Fig. 5(b)]. Besides, ΔZ is inversely proportional to $\widetilde{K}$, which is exactly the trend of Eq. (26). Hence, $\widetilde{K}$ is able to well represent the overall bending stiffness. Meanwhile, it is reasonable to assume that ΔZ is proportional to the deformed deflection of the trailing edge of the plate $w(1)$. It should be noted that the real load distribution along the plate is complex and case-dependent. Hence, in the following discussion, $\widetilde{K}$ will be used as a key parameter to analyze the performances of different plates with typical non-uniformly rigidity distributions.

1. Propulsive performance with $\widetilde{K}$

In terms of $\widetilde{K}$, the mean propulsive velocity, input work, and propulsive efficiency are replotted. From Fig. 6(a), it is seen that for the flapping plates with typical non-uniformly stiffness distributions, the variation trend of propulsive velocity U with $\widetilde{K}$ is consistent with that of the uniform case. There is a common optimal $\widetilde{K} \approx 4$ at which each plate achieves its own largest U. Besides, among all plates, the plate of the GD pattern with the largest standard deviation ("exp 2 ↑") achieves the largest U at the common optimal $\widetilde{K}$. It is noticed that we have only normalized the parameter K, not the propulsive characteristics.

Now, we can compare the propulsive performances of different plates with typical distributions at a specific $\widetilde{K}$. When $\widetilde{K}$ is small, there are significant propulsive performance discrepancies due to the different rigidity distribution. When $\widetilde{K}$ is large, all curves of the typical rigidity distributions almost collapse together. Since the thrust is mainly induced by the leading-edge vortex[26] instead of the deformation when the plates are rigid, the influence of stiffness distribution becomes weak.

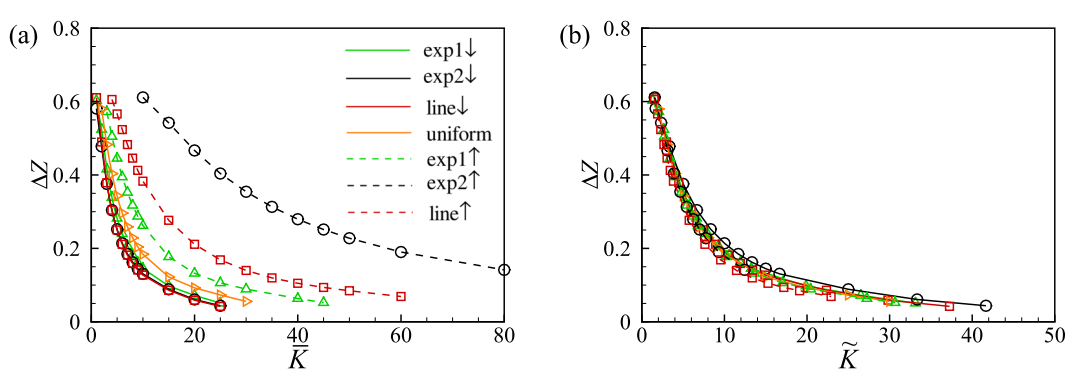

FIG. 5. The maximum displacement difference ΔZ as a function of (a) the mean bending stiffness $\overline{K}$. (b) ΔZ as a function of the normalized bending stiffness $\widetilde{K}$ for different stiffness distribution patterns.

Published under license by AIP Publishing

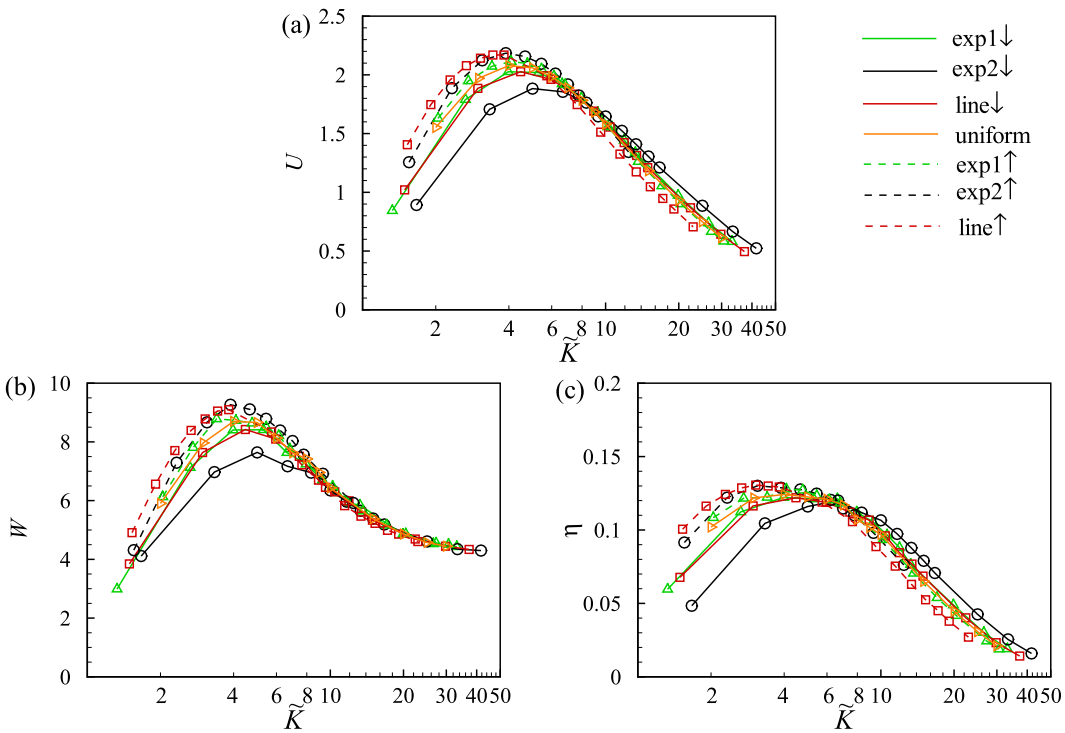

FIG. 6. Propulsive velocity U (a), input work W (b), and propulsive efficiency η (c) as functions of $\widetilde{K}$ for different non-uniformly stiffness distributions.

The input work W and propulsive efficiency η as functions of $\widetilde{K}$ are also shown in Figs. 6(b) and 6(c). Their change trends with different stiffness distributions at small, moderate, and large $\widetilde{K}$ are approximately consistent with that of U in Fig. 6(a). At $\widetilde{K} \approx 4$, the plates also achieve their highest efficiency.

Therefore, based on the normalized rigidity $\widetilde{K}$, we find a common optimal $\widetilde{K} \approx 4$ at which each kind of plate achieves its own best performance. Moreover, the plate of the GD pattern with the largest standard deviation ("exp 2 ↑") is identified to reach the best performance. Compared with the uniform case, the velocity and efficiency of the exp 2 ↑ plate at optimal $\widetilde{K} \approx 4$ are increased by 3% and 4%, respectively. Compared with the exp 2 ↓ case, the velocity and efficiency are increased by 8% and 4.2%, respectively.

2. Deformation and bending energy

The effect of rigidity distribution on deformation and bending energy is investigated. First, the passive pitching angle and the phase lag are analyzed. The passive pitching angle is the result of the interaction between the flexible plate and fluid.[59,60] Figure 7(a) shows

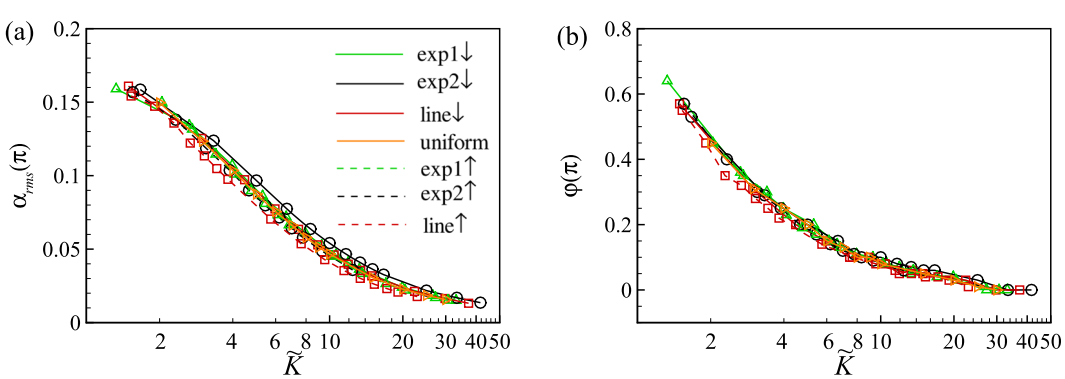

FIG. 7. Profiles of (a) the rms value of passive pitching angles α_{rms} and (b) phase lags φ on the spanwise symmetry plane between the trailing and leading edges of the plate.

Published under license by AIP Publishing

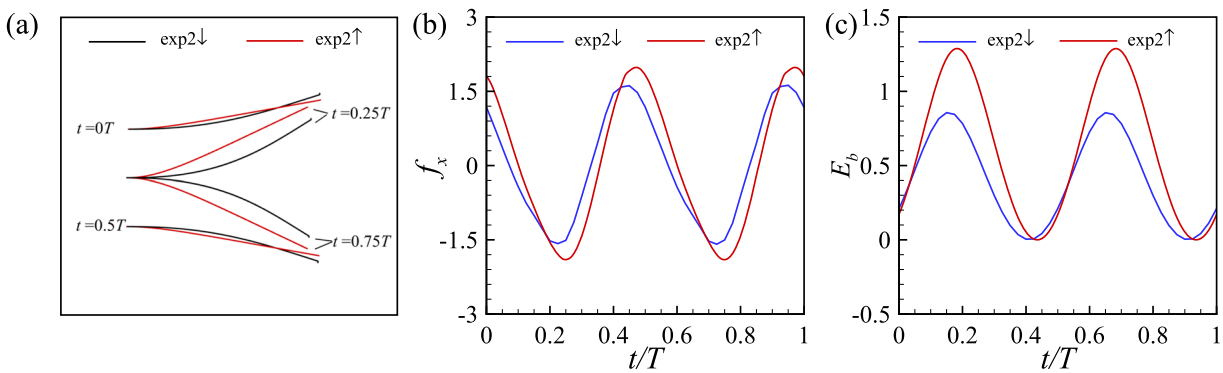

FIG. 8. (a) Plate deformation shape on the spanwise symmetry plane at four instances during one flapping cycle. (b) Evolution of the non-dimensional horizontal force F_x and (c) the bending energy E_b for cases of exp 2 ↓ and exp 2 ↑ at $\widetilde{K} \approx 4$.

the root-mean-square (rms) value of the passive pitching angle α_{rms} during one flapping period for all plates, which is caused by the delayed movement of the free end of the plate relative to the constrained end. It is seen that a small $\widetilde{K}$ leads to a large pitching angle α_{rms}, while a large $\widetilde{K}$ results in a small α_{rms}. All curves for different stiffness distributions collapse together. In other words, at a specific $\widetilde{K}$, the overall α_{rms}s in all cases with different stiffness distributions are nearly identical. Thus, the different propulsive performance at a fixed $\widetilde{K}$ is attributed to the specific local deformation style from the leading to the trailing edge.

Figure 7(b) shows that the variation trend of phase lag is similar to that of α_{rms}. The previous study has indicated that for a flexible plate, the optimal $\varphi \approx 0.25\pi$ would boost the propulsive performance significantly.[61] Figure 7(b) shows that at the optimal overall rigidity $\widetilde{K} \approx 4$, $\varphi \approx 0.25\pi$. Our result is well consistent with that in the work of Ramananarivo *et al.*[61]

Furthermore, the forces acting on the plate and the bending energy of the plate are investigated. Here, we focus on the comparison of the optimal propulsive performance for typical non-uniform stiffness distributions. The cases of $\widetilde{K} \approx 4$ are chosen to analyze since they achieve the best performance. Moreover, the two typical exp 2 ↑ and exp 2 ↓ distributions are analyzed.

The shapes of the plates at several typical instances during one flapping cycle are shown in Fig. 8(a). Due to softer head and harder tail, during the downstroke period from $t/T = 0$ to 0.25, the deformation of the exp 2 ↑ plate is concentrated on its head. It is seen from Fig. 8(b) that at $t/T \approx 0.25$, the curves of F_x reach a valley and are negative. In other words, two plates experience their maximum thrust. The thrust in the case exp 2 ↑ is larger than that in the case exp 2 ↓. Furthermore, the plate in the case exp 2 ↑ gets a larger bending energy [Fig. 8(c)]. A larger bending energy of the plate may also potentially be converted into the kinetic energy of propulsion. The behavior of upstroke is similar to that of the downstroke. Hence, the case of exp 2 ↑ may have a larger U. Thus, the self-propulsive performance is highly related to the deformation distribution, which directly depends on the stiffness distribution.

3. Vortical structure and pressure distribution

To better understand the inherent mechanism in the cases of the DD and GD distributions, i.e., the above two typical cases with exp 2 ↓ and exp 2 ↑ at $\widetilde{K} = 4$, the connection between the vortical structures and the forces on the plate is investigated. For comparison, the uniform case is also included.

The snapshots of spanwise vorticity (ω_y) and pressure distribution along the two side surfaces on the spanwise symmetry planes for the plates are shown in Figs. 9 and 10, respectively.

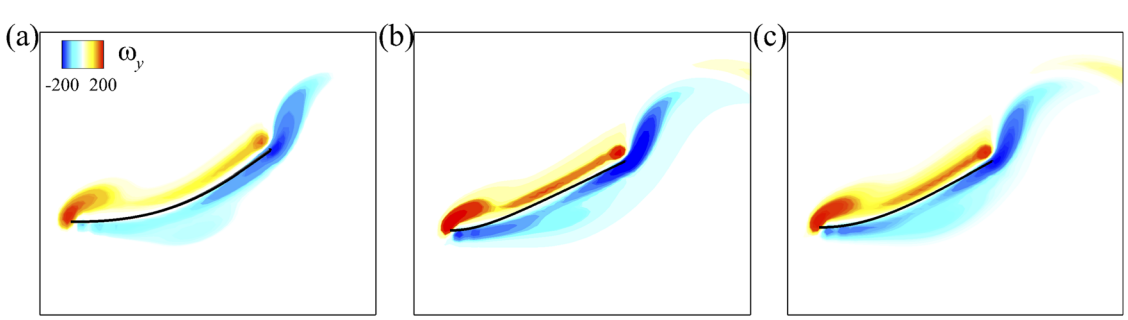

FIG. 9. Snapshots of instantaneous spanwise vorticity (ω_y) on the spanwise symmetry planes for the plates of (a) exp 2 ↓, (b) exp 2 ↑, and (c) uniform case with the optimal $\widetilde{K}$ at the moment when each case achieves its own largest thrust.

Published under license by AIP Publishing

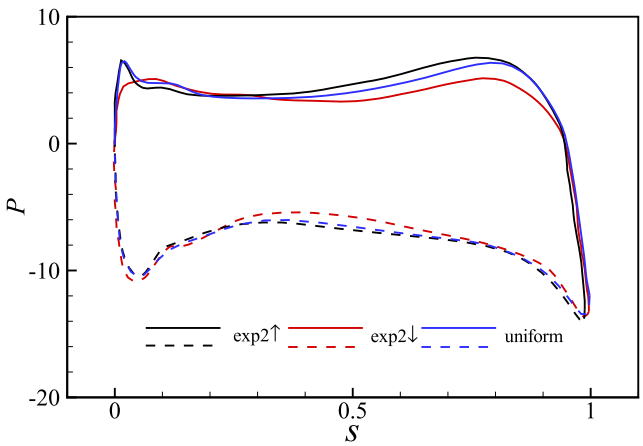

FIG. 10. Pressure distribution along the two side surfaces of a plate on the spanwise symmetry plane at the moment when each case achieves its own largest thrust. The solid and dashed lines represent the distribution on the lower and upper surface of the plate, respectively.

The snapshots are taken at the moment when the maximal thrust appears in each case, i.e., $t/T = 0.225$ in the case of exp 2 ↓ and $t/T = 0.25$ in the cases of exp 2 ↑ and uniform plate. At these moments, the plates are flapping downward and the vortices are generated at the leading edge and then convected to the trailing-edge. The vortex shedding patterns in the three cases look similar except that the vorticity magnitude of case exp 2 ↓ is smaller. We can see that at the moment, the plate of exp 2 ↑ has an obvious bending from its head but the plate of exp 2 ↓ has one from the central region. Different stiffness distributions lead to the deformation discrepancy, resulting in the vorticity discrepancy.

From the pressure distributions (see Fig. 10), we can see that at the moment, the pressure on the lower side of the plate is higher than that on the upper side. The pressure on the upper surface (the dashed lines) looks similar and that in the case of exp 2 ↓ is slightly higher. For the lower surface, the pressure distribution is significantly different. The pressure on the middle and posterior portion of case exp 2 ↓ is the smallest, which may be due to its smaller vorticity magnitude in the lower surface.

The vortices play a dominant role in the thrust generation of the plate.[62] The larger vorticity magnitude and the larger pressure difference between the upper and lower surfaces are favorable to generate a large thrust force. Hence, the thrust force of case exp 2 ↑ is enhanced. The GD case seems favorable to improve the propulsive performance.

C. Force analysis

The forces experienced by the plates are analyzed to reveal the deformation and propulsion mechanism. Previous studies on the flapping flexible wing and plate[61,63] have indicated that the flexible deformation plays an important role in the thrust and drag. Here, we will explore quantitatively the flexible deformation influences on the distribution of thrust.

The jump in the fluid force across the plate on a Lagrangian point, i.e., $\boldsymbol{F}_s$, can be decomposed into two parts: one is the normal force $\boldsymbol{F}_n$ in which the pressure component dominates and the other is the tangential force $\boldsymbol{F}_\tau$, which comes from the viscous effects. These forces are defined as

$$\boldsymbol{F}^n = (\boldsymbol{F}_s \cdot \boldsymbol{n})\boldsymbol{n} = (\boldsymbol{F}_x^n, \boldsymbol{F}_y^n, \boldsymbol{F}_z^n), \tag{28}$$

$$\boldsymbol{F}^\tau = \boldsymbol{F}_s - \boldsymbol{F}^n = (\boldsymbol{F}_x^\tau, \boldsymbol{F}_y^\tau, \boldsymbol{F}_z^\tau), \tag{29}$$

where $\boldsymbol{n}$ and $\boldsymbol{\tau}$ are the unit normal and tangential vectors, respectively, as shown in Fig. 11(a).

The deformation and thrust in the cases of the uniform exp 2 ↓ and exp 2 ↑ distributions are analyzed for $\widetilde{K} = 4$. The local slope, normal force, and x component of the normal force along the chord of plate are shown in Figs. 11(b)–11(d), respectively. Due to the actuation at the leading edge, a heavy load, i.e., a large normal force $\boldsymbol{F}_n$, occurs [see Fig. 11(c)]. For the trailing-edge, there is a low-pressure area near the vortical flow region (see Fig. 9), which contributes to a small normal force $\boldsymbol{F}_n$ in the three cases.

For the exp 2 ↓ plate, Figs. 11(b) and 11(c) show that in the anterior portion, its local slope is the smallest and $|\boldsymbol{F}^n|$ along the chord is also small. All these features lead to a smaller $\boldsymbol{F}_x^n$ in the anterior part. Although in the posterior part, the exp 2 ↓ plate experiences the largest bending deformation among the three cases, a smaller $|\boldsymbol{F}^n|$ in the part results in a smaller thrust $\boldsymbol{F}_x^n$ contributed by the normal force. Hence, the overall thrust force $\overline{\boldsymbol{F}_x^n}$ of the case exp 2 ↓ is the smallest [see Fig. 11(d)].

For the exp 2 ↑ plate, Figs. 11(b) and 11(c) show that the local slope along the anterior portion is the largest and $|\boldsymbol{F}^n|$ along the plate is also slightly larger than those of the other two cases. These features lead to a larger $\boldsymbol{F}_x^n$ in the anterior part. Although the exp 2 ↑ plate experiences a smaller bending deformation in the posterior part, the negative effect may be weakened by the relatively larger $|\boldsymbol{F}^n|$. Hence, the overall thrust force $\overline{\boldsymbol{F}_x^n}$ in the case of exp 2 ↑ is the largest among the three cases [see Fig. 11(d)].

Under the circumstances of an identical ΔZ, a larger bending deformation in the anterior part for the GD pattern is preferred to enhance the self-propulsive performance by a larger $\overline{\boldsymbol{F}_x^n}$. In other words, flexibility focusing on the heaving plate's front is favorable. The front flexibility focusing seems consistent with the results in the literature. Peng *et al.*[40] emphasized that the favorable flexibility distribution depends significantly on the precise boundary condition at the actuation end. The mechanical tethering condition can qualitatively modify the optimal flexibility arrangement of a driven filament. As an example, a heaving clamped filament prefers more flexibility at the actuation end,[36] which is analogous to the front flexible situation in our cases. In the architecture of flapping-wing systems found in nature, focusing flexibility seems helpful to enhance the performance.[36] For example, by incorporating a torsional spring into ornithopters, these systems might boost their thrust production during the acceleration phase and thus reduce the time needed to reach steady flight. Torsional flexibility at the wing–body joint for insect wings is another application to generate enough lift during hovering, ensuring the passive pitching motion of the wings without the aid of the muscles.[64,65]

Although the decreasing stiffness distribution outperforms the uniform distribution in many previous literatures,[35,37,45] the comparison style that they performed does not exclude the effect of overall rigidity ($\widetilde{K}$) because $\widetilde{K}$ of the decreasing distribution (DD)

Published under license by AIP Publishing

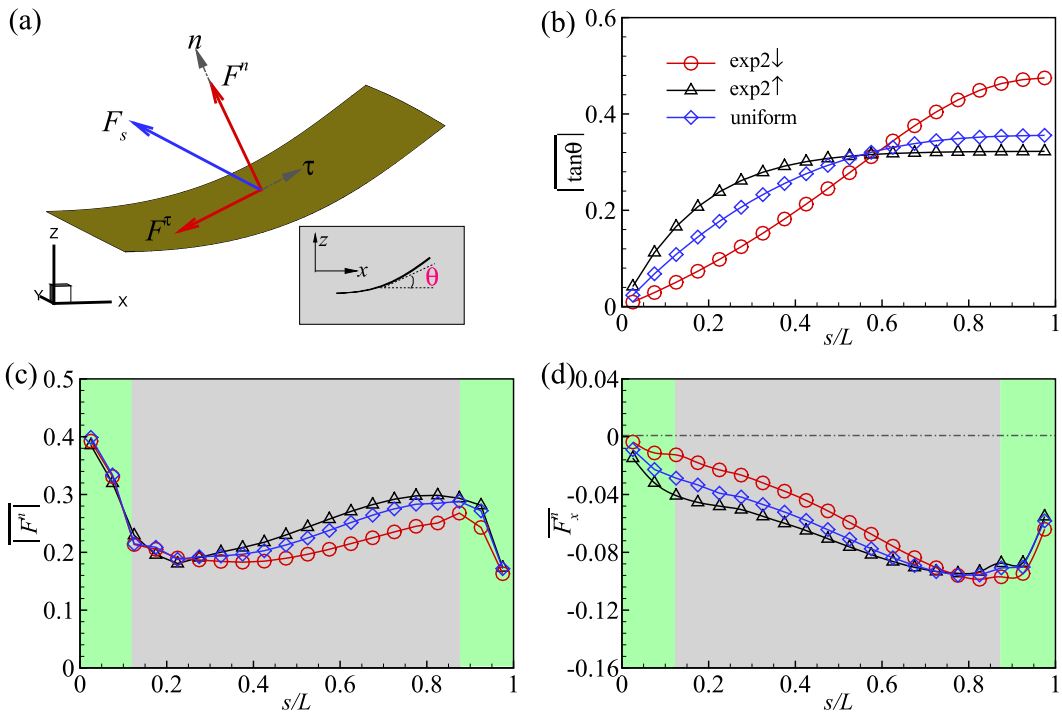

FIG. 11. (a) Schematic diagram for force decomposition: τ and n denote the local tangential and normal directions, respectively. The inset represents the local deflection angle θ at the Lagrangian point on the spanwise symmetric plane. The local slope and normal force along the chord for the cases of exp 2 ↓ and exp 2 ↑ and uniform patterns ($\widetilde{K} = 4$). (b) Time-averaged absolute slope, (c) time-averaged absolute normal force, and (d) time-averaged F_n^x. The green regions represent the leading and trailing edges.

case is different from that of the uniform case. Obviously, the performance is a function of the rigidity (see Figs. 6 and 11). For example, the DD case with $\widetilde{K} = 5$ would outperform the uniform distribution with $\widetilde{K} = 2$. This is also consistent with our result (see Fig. 6). In our study, we first ensure that the overall rigidities of the DD case and the uniform case are identical. Hence, the comparison style is different from that in Refs. 35, 37, 45, and 66. Our comparison style is more reasonable.

D. Effect of aspect ratio

All of the above results are obtained for the cases with aspect ratio $H = 1$ under the specified heaving actuation. We further examine whether the conclusions about the optimal stiffness distribution are valid for the cases of another aspect ratio under the same actuation. The cases with aspect ratio $H = 4$ are simulated. We focus on the two typical distributions of exp 2 ↑ and exp 2 ↓. The propulsive

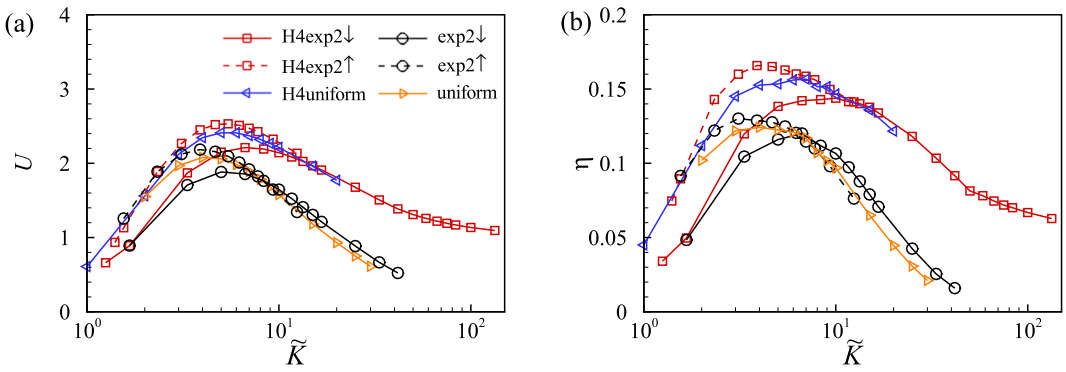

FIG. 12. Propulsive velocity U (a) and propulsive efficiency η (b) as functions of $\widetilde{K}$ for the cases with $H = 4$ and $H = 1$.

Published under license by AIP Publishing

velocity U and propulsive efficiency η as functions of $\widetilde{K}$ for the cases with $H = 4$ and $H = 1$ are presented in Fig. 12.

It is seen that in a small $\widetilde{K}$ region, the variations of the propulsive speed and efficiency vs $\widetilde{K}$ at $H = 4$ are similar to those at $H = 1$. The plate "exp 2 ↑" also achieves the best performance. It means that the propulsive characteristics are almost independent of the aspect ratio and mainly depend on the stiffness distribution and $\widetilde{K}$. Hence, the above conclusions about optimal $\widetilde{K}$ and the flexibility focusing may be still valid for other aspect ratios.

It is also noticed that for moderate and large $\widetilde{K}$, U and η at $H = 4$ are larger than those of $H = 1$. The swimming performance increases as the span of the plate increases, which is consistent with the conclusion in the literature.[18,53] Under the circumstances of moderate and large $\widetilde{K}$, the curves of different stiffness distribution coincide with each other approximately. The plate deformation is diminished and the effect of stiffness distribution on the propulsion becomes weakened.

V. CONCLUDING REMARKS

Self-propulsion of flexible plates is studied numerically to investigate the impact of non-uniform chordwise stiffness distribution on the propulsive performance. Three typical stiffness distributions, including uniform, declining, and growing distributions, are considered. The major conclusions are briefly summarized as follows:

First, the normalized overall bending stiffness $\widetilde{K}$ is derived based on the Euler beam model, which reasonably represents the overall bending stiffness characteristics of the non-uniform plate. The maximum displacement difference ΔZ between the trailing and leading edges is found to be proportional to the analytical deflection of the trailing edge of plate $w(1)$. For all the plates with different stiffness distributions, their best propulsive performances commonly occur at $\widetilde{K} \approx 4$. Moreover, the plate of the GD distribution with the largest standard deviation achieves the best performance among all plates.

The pressure field and the force and deformation along the chord are investigated for the cases at $\widetilde{K} \approx 4$. Our analyses indicate that a larger bending deformation in the anterior part of the plate with the GD distribution leads to a larger thrust force, which is favorable for performance enhancement. These conclusions are also valid for different aspect ratios. It is noticed that the actuation in our numerical simulation is limited to heaving without active pitching. Therefore, the optimal stiffness distribution is only applicable to the pure heaving actuation. An appealing extension of the present findings would be the consideration of the active pitching actuation, so as to compare the different mechanical tethering conditions. The present study may shed some light on a better understanding of hydrodynamic performances of the non-uniform stiffness wings or fins of the propeller of animals in nature.

ACKNOWLEDGMENTS

This work was supported by the Natural Science Foundation of China (NSFC; Grant Nos. 11872064 and 11621202). H.H. was supported by the NSFC (Grant No. 11972342).

DATA AVAILABILITY

The data that support the findings of this study are available from the corresponding author upon reasonable request.

REFERENCES

[1] M. Vanella, T. Fitzgerald, S. Preidikman, E. Balaras, and B. Balachandran, "Influence of flexibility on the aerodynamic performance of a hovering wing," J. Exp. Biol. **212**, 95 (2009).
[2] J. Young, S. M. Walker, R. J. Bomphrey, G. K. Taylor, and A. L. R. Thomas, "Details of insect wing design and deformation enhance aerodynamic function and flight efficiency," Science **325**, 1549 (2009).
[3] R. W. Blake, *Fish Locomotion* (Cambridge University Press, 1983).
[4] A. K. Brodsky, *The Evolution of Insect Flight* (Oxford University Press, 1994).
[5] F. E. Fish and G. V. Lauder, "Passive and active flow control by swimming fishes and mammals," Annu. Rev. Fluid Mech. **38**, 193 (2006).
[6] W. Shyy, Y. Lian, J. Tang, D. Viieru, and H. Liu, *Aerodynamics of Low Reynolds Number Flyers* (Cambridge University Press, 2007).
[7] W. Shyy, H. Aono, S. K. Chimakurthi, P. Trizila, C.-K. Kang, C. E. S. Cesnik, and H. Liu, "Recent progress in flapping wing aerodynamics and aeroelasticity," Prog. Aerosp. Sci. **46**, 284 (2010).
[8] J. J. Videler, *Fish Swimming* (Springer, 2012).
[9] S. Alben, "Optimal flexibility of a flapping appendage in an inviscid fluid," J. Fluid Mech. **614**, 355 (2008).
[10] S. Alben, C. Witt, T. V. Baker, E. Anderson, and G. V. Lauder, "Dynamics of freely swimming flexible foils," Phys. Fluids **24**, 051901 (2012).
[11] M. N. J. Moore, "Analytical results on the role of flexibility in flapping propulsion," J. Fluid Mech. **757**, 599 (2014).
[12] S. Heathcote and I. Gursul, "Flexible flapping airfoil propulsion at low Reynolds numbers," AIAA J. **45**, 1066 (2007).
[13] D. B. Quinn, G. V. Lauder, and A. J. Smits, "Maximizing the efficiency of a flexible propulsor using experimental optimization," J. Fluid Mech. **767**, 430 (2015).
[14] D. Floryan and C. W. Rowley, "Clarifying the relationship between efficiency and resonance for flexible inertial swimmers," J. Fluid Mech. **853**, 271 (2018).
[15] B. Yin and H. Luo, "Effect of wing inertia on hovering performance of flexible flapping wings," Phys. Fluids **22**, 111902 (2010).
[16] C.-K. Kang, H. Aono, C. E. S. Cesnik, and W. Shyy, "Effects of flexibility on the aerodynamic performance of flapping wings," J. Fluid Mech. **689**, 32 (2011).
[17] X. Zhu, G. He, and X. Zhang, "How flexibility affects the wake symmetry properties of a self-propelled plunging foil," J. Fluid Mech. **751**, 164 (2014).
[18] A. P. Hoover, R. Cortez, E. D. Tytell, and L. J. Fauci, "Swimming performance, resonance and shape evolution in heaving flexible panels," J. Fluid Mech. **847**, 386 (2018).
[19] N. Arora, C.-K. Kang, W. Shyy, and A. Gupta, "Analysis of passive flexion in propelling a plunging plate using a torsion spring model," J. Fluid Mech. **857**, 562 (2018).
[20] S. Michelin and S. G. Llewellyn Smith, "Resonance and propulsion performance of a heaving flexible wing," Phys. Fluids **21**, 071902 (2009).
[21] P. A. Dewey, B. M. Boschitsch, K. W. Moored, H. A. Stone, and A. J. Smits, "Scaling laws for the thrust production of flexible pitching panels," J. Fluid Mech. **732**, 29 (2013).
[22] R.-N. Hua, L. Zhu, and X.-Y. Lu, "Locomotion of a flapping flexible plate," Phys. Fluids **25**, 121901 (2013).
[23] G. V. Lauder, J. Lim, R. Shelton, C. Witt, E. Anderson, and J. L. Tangorra, "Robotic models for studying undulatory locomotion in fishes," Mar. Technol. Soc. J. **45**, 41 (2011).
[24] T. Van Buren, D. Floryan, D. Brunner, U. Senturk, and A. J. Smits, "Impact of trailing edge shape on the wake and propulsive performance of pitching panels," Phys. Rev. Fluids **2**, 059901 (2017).
[25] Y. Jin, J.-T. Kim, L. Hong, and L. P. Chamorro, "Flow-induced oscillations of low-aspect-ratio flexible plates with various tip geometries," Phys. Fluids **30**, 097102 (2018).

Published under license by AIP Publishing

[26]C. Zhang, H. Huang, and X.-Y. Lu, "Effect of trailing-edge shape on the self-propulsive performance of heaving flexible plates," J. Fluid Mech. **887**, A7 (2020).
[27]J. Ryu, S. G. Park, W.-X. Huang, and H. J. Sung, "Hydrodynamics of a three-dimensional self-propelled flexible plate," Phys. Fluids **31**, 021902 (2019).
[28]M. J. McHenry, C. A. Pell, and J. H. Long, Jr., "Mechanical control of swimming speed: Stiffness and axial wave form in undulating fish models," J. Exp. Biol. **198**, 2293 (1995).
[29]C. Zuo and H. Jiang, "Modeling and analysis of a swimming tincaeus with bio-inspired stiffness profile," in 2015 IEEE International Conference on Robotics and Biomimetics, 2015.
[30]A. K. Kancharala and M. K. Philen, "Optimal chordwise stiffness profiles of self-propelled flapping fins," Bioinspiration Biomimetics **11**, 056016 (2016).
[31]H. Luo, D. Hu, S. S. Das, J. Song, and J. Doyle, "Toward high-fidelity modeling of the fluid-structure interaction for insect wings," in 50th AIAA Aerospace Sciences Meeting including the New Horizons Forum and Aerospace Exposition, 2012.
[32]A. Shahzad, F.-B. Tian, J. Young, and J. C. S. Lai, "Effects of hawkmoth-like flexibility on the aerodynamic performance of flapping wings with different shapes and aspect ratios," Phys. Fluids **30**, 091902 (2018).
[33]K. N. Lucas, N. Johnson, W. T. Beaulieu, E. Cathcart, G. Tirrell, S. P. Colin, B. J. Gemmell, J. O. Dabiri, and J. H. Costello, "Bending rules for animal propulsion," Nat. Commun. **5**, 3293 (2014).
[34]P. Riggs, A. Bowyer, and J. Vincent, "Advantages of a biomimetic stiffness profile in pitching flexible fin propulsion," J. Bionic Eng. **7**, 113 (2010).
[35]K. N. Lucas, P. J. M. Thornycroft, B. J. Gemmell, S. P. Colin, J. H. Costello, and G. V. Lauder, "Effects of non-uniform stiffness on the swimming performance of a passively-flexing, fish-like foil model," Bioinspiration Biomimetics **10**, 056019 (2015).
[36]M. N. J. Moore, "Torsional spring is the optimal flexibility arrangement for thrust production of a flapping wing," Phys. Fluids **27**, 091701 (2015).
[37]K. Shoele and Q. Zhu, "Leading edge strengthening and the propulsion performance of flexible ray fins," J. Fluid Mech. **693**, 402 (2012).
[38]K. Shoele and Q. Zhu, "Performance of a wing with nonuniform flexibility in hovering flight," Phys. Fluids **25**, 041901 (2013).
[39]T. T. Nguyen, D. Shyam Sundar, K. S. Yeo, and T. T. Lim, "Modeling and analysis of insect-like flexible wings at low Reynolds number," J. Fluids Struct. **62**, 294 (2016).
[40]Z. Peng, G. J. Elfring, and O. S. Pak, "Maximizing propulsive thrust of a driven filament at low Reynolds number via variable flexibility," Soft Matter **13**, 2339 (2017).
[41]Q. Zhu, "Numerical simulation of a flapping foil with chordwise or spanwise flexibility," AIAA J. **45**, 2448 (2007).
[42]S. Heathcote, Z. Wang, and I. Gursul, "Effect of spanwise flexibility on flapping wing propulsion," J. Fluids Struct. **24**, 183 (2008).
[43]Q. Zhu and X. Bi, "Effects of stiffness distribution and spanwise deformation on the dynamics of a ray-supported caudal fin," Bioinspiration Biomimetics **12**, 026011 (2017).
[44]Y. Luo, Q. Xiao, G. Shi, L. Wen, D. Chen, and G. Pan, "A fluid-structure interaction solver for the study on a passively deformed fish fin with non-uniformly distributed stiffness," J. Fluids Struct. **92**, 102778 (2020).
[45]Y. Luo, Q. Xiao, G. Shi, G. Pan, and D. Chen, "The effect of variable stiffness of tuna-like fish body and fin on swimming performance," Bioinspiration Biomimetics **16**, 016003 (2020).
[46]Z.-R. Peng, H. Huang, and X.-Y. Lu, "Collective locomotion of two closely spaced self-propelled flapping plates," J. Fluid Mech. **849**, 1068 (2018).
[47]Z.-R. Peng, H. Huang, and X.-Y. Lu, "Collective locomotion of two self-propelled flapping plates with different propulsive capacities," Phys. Fluids **30**, 111901 (2018).
[48]B. S. H. Connell and D. K. P. Yue, "Flapping dynamics of a flag in a uniform stream," J. Fluid Mech. **581**, 33 (2007).
[49]S. Chen and G. D. Doolen, "Lattice Boltzmann method for fluid flows," Annu. Rev. Fluid Mech. **30**, 329 (1998).
[50]J. F. Doyle, *Nonlinear Analysis of Thin-Walled Structures: Statics, Dynamics, and Stability* (Springer, 2001).
[51]C. S. Peskin, "The immersed boundary method," Acta Numer. **11**, 479 (2002).
[52]R. Mittal and G. Iaccarino, "Immersed boundary methods," Annu. Rev. Fluid Mech. **37**, 239 (2005).
[53]C. Tang, H. Huang, P. Gao, and X.-Y. Lu, "Self-propulsion of a flapping flexible plate near the ground," Phys. Rev. E. **94**, 033113 (2016).
[54]D. d'Humières, I. Ginzburg, M. Krafczyk, P. Lallemand, and L. Luo, "Multiple-relaxation-time lattice Boltzmann models in three dimensions," Philos. Trans. R. Soc., A **360**, 437 (2002).
[55]Z. Guo, C. Zheng, and B. Shi, "Discrete lattice effects on the forcing term in the lattice Boltzmann method," Phys. Rev. E. **65**, 046308 (2002).
[56]R.-N. Hua, L. Zhu, and X.-Y. Lu, "Dynamics of fluid flow over a circular flexible plate," J. Fluid Mech. **759**, 56 (2014).
[57]L. Wang, Z. Fang, R.-N. Hua, and Z.-R. Peng, "Numerical simulations of an inverted flexible plate in linear shear flows," Phys. Fluids **32**, 043104 (2020).
[58]W.-X. Huang and H. J. Sung, "Three-dimensional simulation of a flapping flag in a uniform flow," J. Fluid Mech. **653**, 301 (2010).
[59]J. M. Anderson, K. Streitlien, D. S. Barrett, and M. S. Triantafyllou, "Oscillating foils of high propulsive efficiency," J. Fluid Mech. **360**, 41 (1998).
[60]M. S. Triantafyllou, G. S. Triantafyllou, and D. K. P. Yue, "Hydrodynamics of fishlike swimming," Annu. Rev. Fluid Mech. **32**, 33 (2000).
[61]S. Ramananarivo, R. Godoy-Diana, and B. Thiria, "Rather than resonance, flapping wing flyers may play on aerodynamics to improve performance," Proc. Natl. Acad. Sci. U. S. A. **108**, 5964 (2011).
[62]G.-J. Li and X.-Y. Lu, "Force and power of flapping plates in a fluid," J. Fluid Mech. **712**, 598 (2012).
[63]B. Thiria and R. Godoy-Diana, "How wing compliance drives the efficiency of self-propelled flapping flyers," Phys. Rev. E. **82**, 015303 (2010).
[64]A. R. Ennos, "The importance of torsion in the design of insect wings," J. Exp. Biol. **140**, 137 (1988).
[65]A. J. Bergou, S. Xu, and Z. J. Wang, "Passive wing pitch reversal in insect flight," J. Fluid Mech. **591**, 321 (2007).
[66]N. S. Reddy, S. Sen, and C. Har, "Effect of flexural stiffness distribution of a fin on propulsion performance," Mech. Mach. Theory **129**, 218 (2018).

Published under license by AIP Publishing